Supporting Information for: Helical Hole State in Multiple Conduction Modes in Ge/Si Core/Shell Nanowire

Jian Sun,[*,†,‡] Russell S. Deacon,[†,¶] Rui Wang,[†] Jun Yao,[§,‖] Charles M. Lieber,[§,⊥] and Koji Ishibashi[†,¶]

†*Advanced Device Laboratory, RIKEN, 2-1 Hirosawa,Wako, Saitama 351-0198, Japan*

‡*School of Physical Science and Electronics, Central South University, Changsha 410083, China*

¶*Center for Emergent Matter Science, RIKEN, Wako, Saitama 351-0198, Japan*

§*Deparment of Chemistry and Chemical Biology, Harvard University, Cambridge, MA 02138, USA*

‖*Department of Electrical and Computer Engineering, Institute for Applied Life Sciences, University of Massachusetts, Amherst, MA 01003, USA*

⊥*School of Engineering and Applied Sciences, Harvard University, Cambridge, MA 02138, USA*

E-mail: jian.sun@riken.jp

Fax: +81-48-462-4659

I. Quantized conductance traces

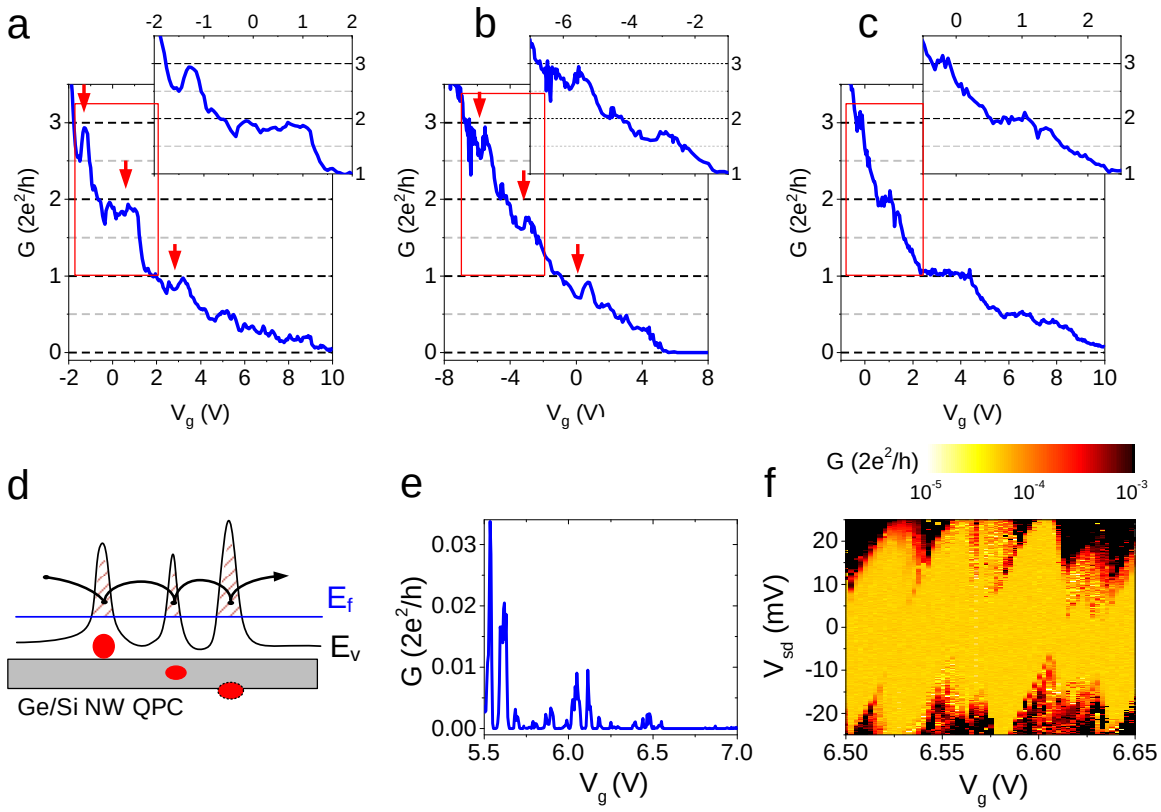

Figure S1: (a) and (b) Conductance traces with no B-field application measured before and after the temperature cycle at 7.5 K without DC bias, respectively. (c) Conductance traces with no B-field application measured before temperature cycle at 12 K with 1 mV DC bias. The red arrows indicate the re-entrant conductance features observed on the plateaus of each mode. Insets show the zoomed-in details of the red boxes. (d) A schematic showing the quantum-dot like transport in the NW due to tunnelling through isolated localized charge puddles. The Blue line denoted with E_f indicates the Fermi energy. The distribution of the bottom of the lowest sub-valence band in the NW is indicated by the black line E_v. (e) Zoomed-in plot of (b) in the "pinch-off" regime in which clear Coulomb oscillations are observed. (f) Charge stability measurement of the QPC device in the "pinch-off" regime.

In Figs. S1a and b, we plot the conductance traces measured between pinch-off and the 3rd mode in the device presented in main text before and after the temperature cycle, respectively. The red arrows indicate the re-entrant conductance features appearing on each plateau. Note here, a constant background resistance is subtracted from the as-measured data, which includes the contact resistance and resistances of the onset potential segments

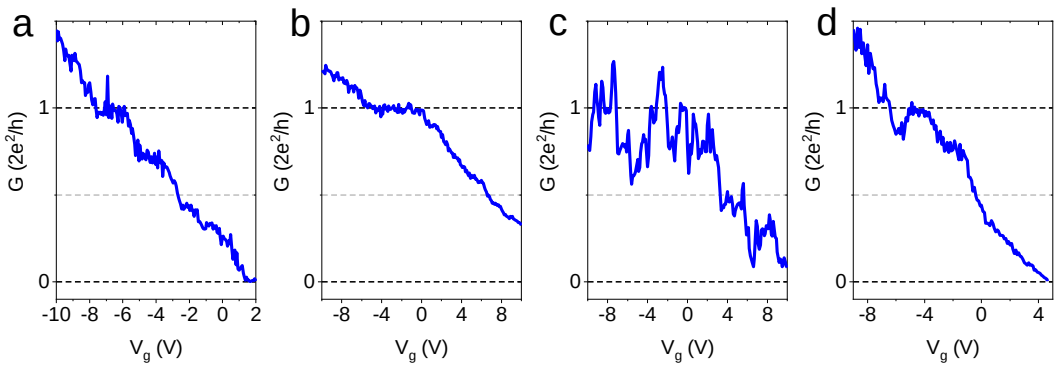

Figure S2: Conductance traces with no B-field application measured in QPC devices different from that in the main text. (a) 260 nm-long QPC, and (b) 255 nm-long QPC, made on the same nanowire of the one in Fig. S1a; (c) a 250 nm-long QPC fabricated on a thicker nanowire with Ge core of $\Phi \sim 18$ nm; (d) 300 nm-long QPC with Ge core of $\Phi \sim 18$ nm, same as the one presented in SI section V.

(λ). The resistance difference between the adjacent plateaus is known as a unique value. For example, the resistance difference between 1$^{\text{st}}$ and 2$^{\text{nd}}$ plateau is 6.453 kΩ, and between 2$^{\text{nd}}$ and 3$^{\text{rd}}$ plateau is 2.151 kΩ. By verifying this, we can confirm the number of mode for each recognized plateau. Then, a background resistance value can be determined and subtracted from the measured data. The background resistance is about ~ 25 kΩ for this specific device.

By comparing (a) and (b), we know that the temperature cycle induces n-doping behaviour and causes a ~ 6 V negative shift of the pinch-off. Due to the presence of zero-field gap, the quantized conductance plateaus are always cut into two segments. In order to give a better presentation of flat quantized conductance plateau, we did the conductance measurement at high temperature of 12 K and a finite DC bias of 1 mV before the temperature cycle. The data is plotted in Fig. S1c. Under such circumstance, the zero-field gap feature vanishes, resulting in the more pronounced flat plateaus. In all three measurements, a e^2/h plateau is observed (at $V_g \sim 5$ V in a and at $V_g \sim 3$ V in b) and is assumed to arise from an electron-electron interaction induced spin polarized sub-band as descried in the main text. When approaching pinch-off, we observe conductance features arising from localization in the QPC channel. We ascribe these features to localized charge puddles in the NW caused by potential fluctuations, likely originating from surface contamination, material defects, and

substrate defects. These charge puddles appear as a multiple quantum dot like structure in the transport measurements as presented in Figs. S1c. When Fermi level E_f leaves the lowest sub-band E_v a transition occurs from quasi-ballistic to quantum-dot like transport instead of an abrupt pinch off behaviour. As a strong experimental evidence supporting this scenario, clear Coulomb oscillations are observed in the pinch-off regime as presented in Fig. S1d. Additionally, well defined diamond-like patterns are noted in its charge stability measurement (Fig. S1e).

We searched for quantized conductance and re-entrant conductance features in various QPC devices with different geometries. While re-entrant conductance features were only found in a few cases, quantized conductance features can be observed in a number of devices. We plot additional measurements of conductance traces in other QPCs in fig. S2. Figs. S2a and b are the measurements in the QPCs made on the same nanowire as fig. S1 with lengths of 260 nm and 255 nm, respectively. Both show only one plateau of the 1^{st} mode in the measurable gate range. Fig. S2c shows the conductance measurement of a short QPC of 250 nm fabricated on a thicker nanowire with Ge core of $\Phi \sim 18$ nm without removing the background resistance, as the conductance trace is masked by the fluctuations and quantized plateaus cannot be identified. In these devices, the onset potential length is possibly far from the optimal Zeeman length, or the contacts may have insufficient transparency. Finally, fig.S2d shows conductance trace measured in a QPC with length of 300 nm and Ge core diameter of 18 nm. Re-entrant conductance feature is also found in this QPC, which is presented later in SI section V.

II. Temperature dependence of the measurements

Fig. S3 plots the quantized conductance measurements at varied temperatures. At the base temperature of 1.4 K, the severe noise-like oscillations in conductance are observed, making the identification of quantized conductance and helical really difficult. We note that

these oscillations are conductance fluctuations combined with a possible effect of the Fabry-Pérot interference. As the temperature is raised, the main features appear at the same gate voltages. Most importantly, they are much suppressed. At 7.5 K, the quantized conductance and re-entrant conductance feature are recognized.

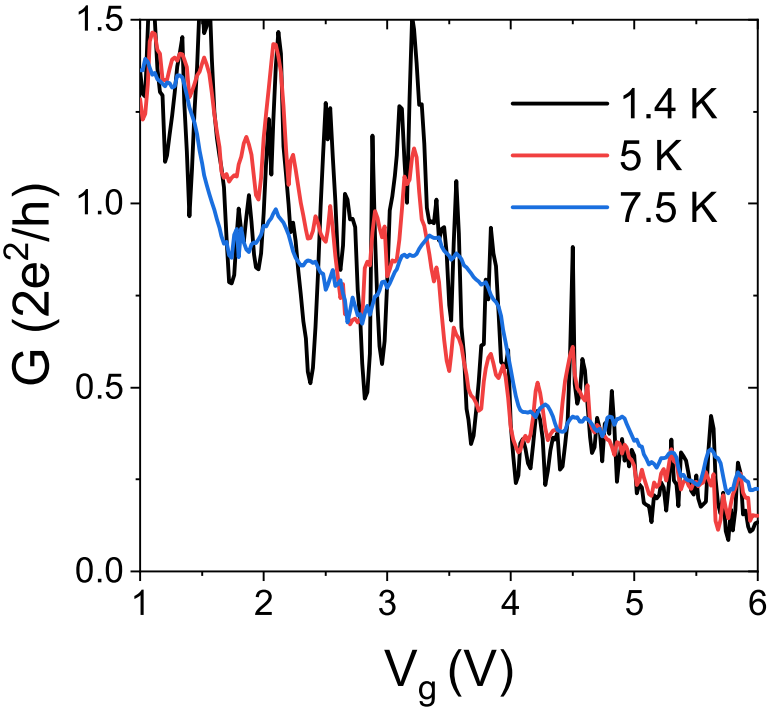

Figure S3: Temperature dependence of the measurements of the 1^{st} quantized conductance plateau (Device 1).

III. Simulation of the effective QPC length

As described by Rainis et al.,[1] in order to identify the helical gap in the quantized conductance measurement, an adiabatic potential profile in the QPC channel must be fulfilled, *i.e.* the realistic onset potential length λ should be close to an optimal value λ^*. For either too small or too large λ, masking effects are present due to different mechanisms, making the re-entrant conductance feature difficult or impossible to observe. Additionally, due to the onset potential profile, the effective QPC length l_{QPC} is shorter than the designed channel length l_{ch}, $l_{QPC} = l_{ch} - 2\lambda$. We carry out a finite element simulation to estimate the effec-

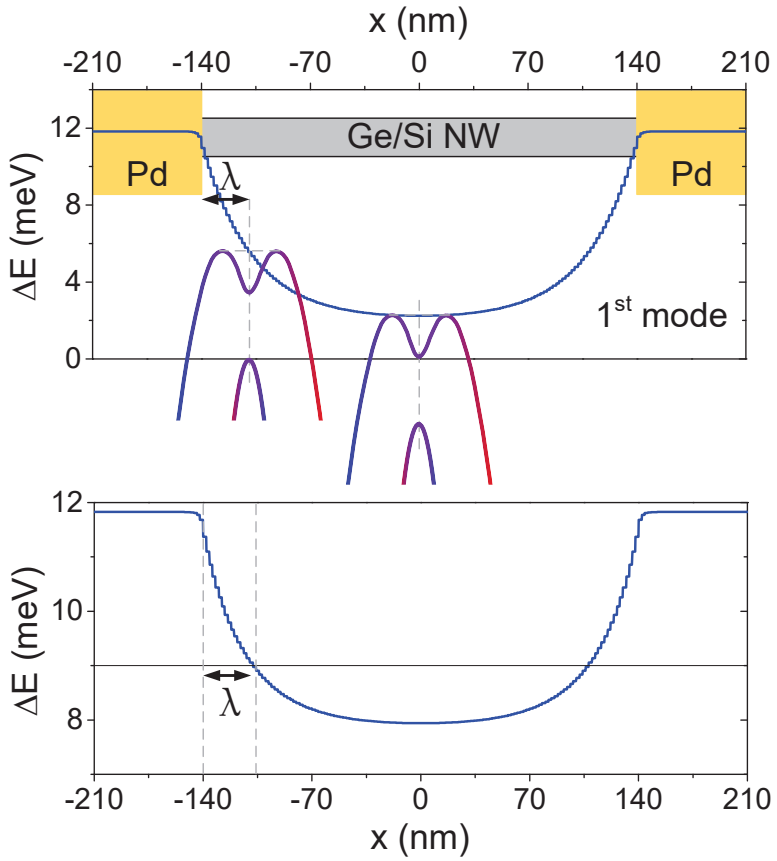

Figure S4: Simulated energy distribution in Ge/Si NW in the 1st mode (upper) and in the 2nd mode (lower), respectively.

tive QPC length using the commercial software COMSOL Multiphysics. The distribution of the Fermi energy and the lowest valence band energy along the NW are calculated using a Schrödinger-Poisson solver.

In Fig. S4, we plot the result for a QPC with two Pd contacts spaced 280 nm apart, a 30 nm dielectric and a global gate. A small potential value of -0.2 V is assigned to both contacts to simulate the work function misalignment between Pd and Ge. Here we define the term ΔE as the energy difference between the top of the lowest valence band and the Fermi level. The upper plot shows the ΔE distribution in the NW for the 1st mode. In the center of the NW, ΔE is around 2 meV, *i.e.* the Fermi level is entering the helical gap. At the location of 113 nm away from the center of the fabricated channel length, ΔE is found to be 6 meV, indicating that the Fermi level leaves the helical gap. The portion of the NW

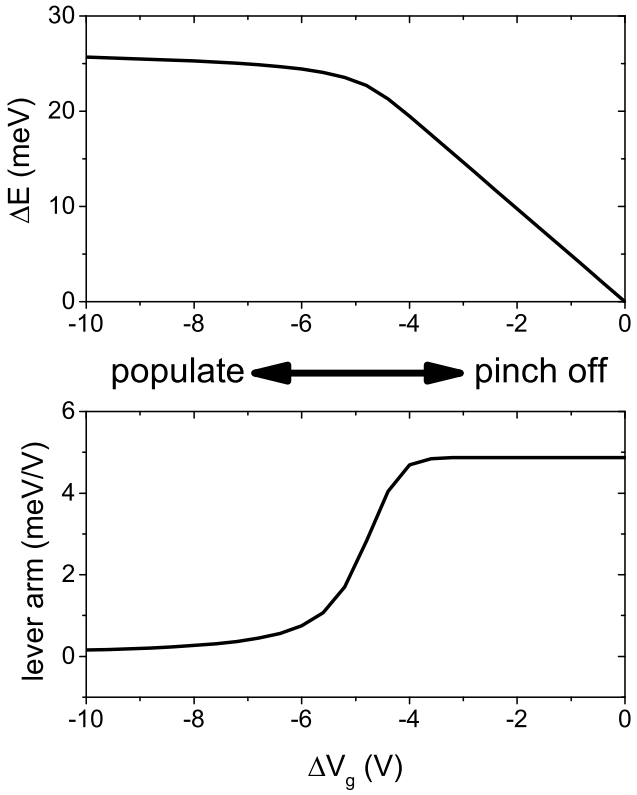

Figure S5: Simulated relative energy change and gate lever arm in NW as a function of gate voltage.

outside this region has higher sub-bands occupied and is not considered as part of the QPC. Using this crude assessment we estimate that λ is around 28 nm. Kammhuber *et al.,* showed that λ does not change significantly with gate voltage using a global gate.[2] Using the same method, we estimate the effective QPC length when the NW is in the 2^{nd} mode. The value of λ is calculated as 33 nm and the effective QPC length is about 220 nm, similar to values found for the 1^{st} mode. The helical gap size used for the analysis here is that determined in experiment in the main text. Both of the λ values estimated here are comparable to the optimal $\lambda^* = 39$ nm found in the main text, ensuring a good visibility of the helical gap feature.

Using the finite element tool, we are also able to simulate the dependence of the gate lever-arm on the gate voltage. Fig. S5 plots the relative energy change ΔE as a function of varied gate voltages and its corresponding gate lever arm. When the gate voltage is low, the

NW is close to pinch-off and the lever-arm is almost constant. We observe that the lever-arm decreases significantly with more negative gate voltages as the NW is populated, which is consistent with our experimental findings.

IV. Additional measurements of bias spectroscopy

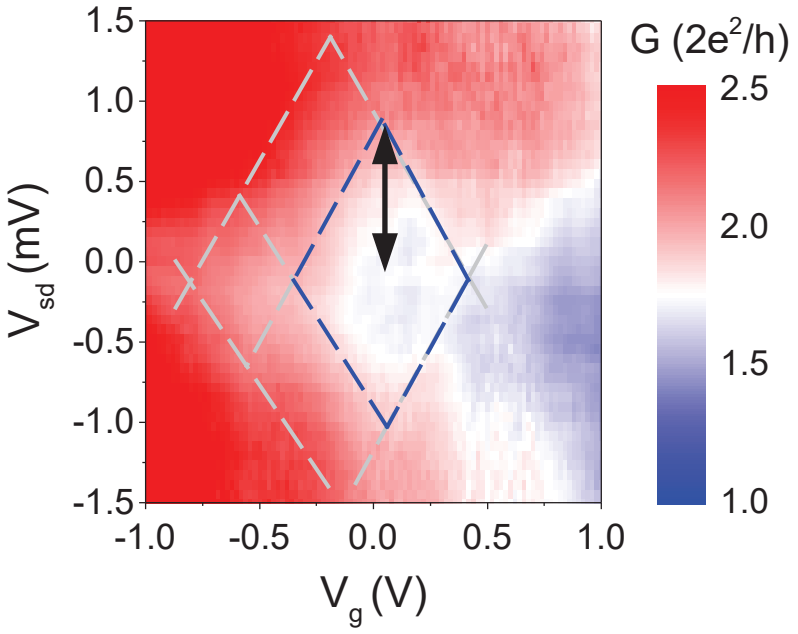

Figure S6: Voltage bias spectroscopy measured in the 2nd mode of the 1st device at 2.5 T. The blue dashed lines indicate the perimeter of the helical gap region, and the black arrow indicate its energy spacing.

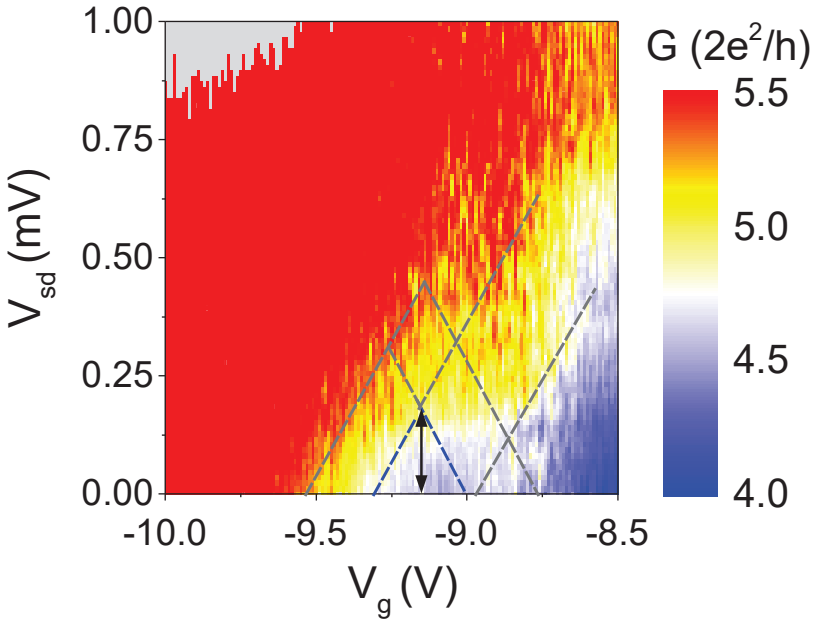

Figure S7: Voltage bias spectroscopy measured in the 5$^{\text{th}}$ mode of the 1st device at 4 T with only positive bias application. The blue dashed lines indicate the perimeter of the helical gap region, and the black arrow indicate its energy spacing.

V. Measurements of a second device

We measure the possible signature of helical gap in a different device, which is built on a nanowire with the diameter of $\sim$ 25 nm, thicker than the 1st nanowire presented in the main text. The channel length is about 300 nm. Figs. S8 and S9 present the magnetic dependence and the bias spectroscopy of the helical gap, respectively. Due to the relative weaker geometric confinement, the subbands are not well quantized with large spacing compared to the device with a thinner wire. Consequently, the measured quantized conductance and helical gap feature are weaker and less pronounced.

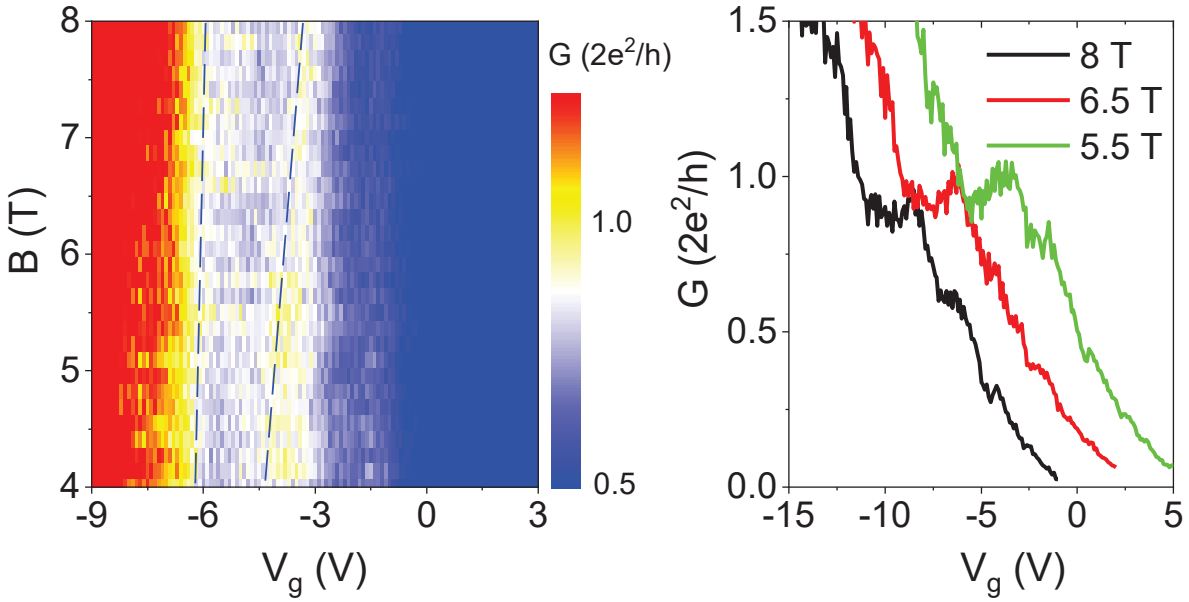

Figure S8: Quantized conductance measured in the 2nd device as a function of B-field, where B is slightly off the perpendicular orientation. Right plot presents the line traces cut from the 2D map at various B. The traces are shifted horizontally for clarity. Using the lever arm of 1.41 meV/V, the landé g factor is estimated as 3.84; pseudo-gap at zero field $E_s = 1.61$ meV; spin-orbit energy $E_{so} = 1.71$ meV.

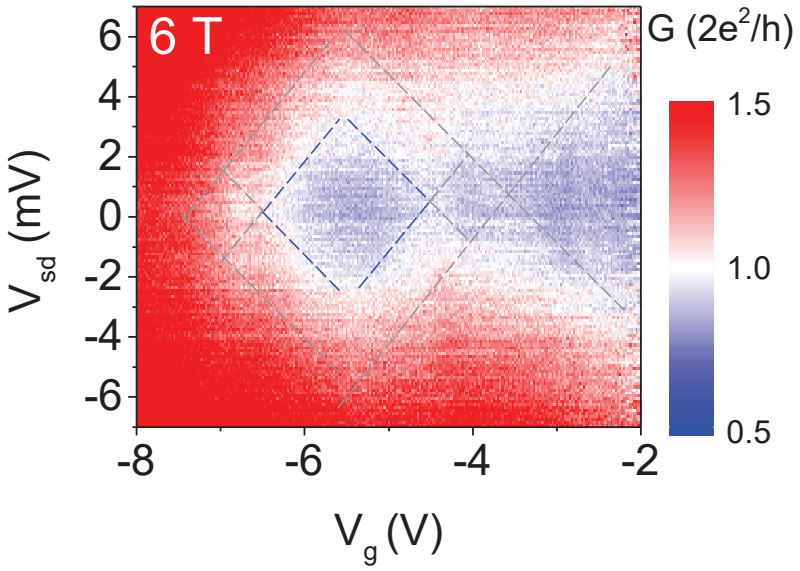

Figure S9: Differential conductance G measured in the 2nd device as a function of V_g and V_{sd} at B of 6 T . Dashed lines are a guide to the eye indicating the conductance plateaus. The blue dashed lines indicate the perimeter of the helical gap region. The gate lever arm is therefore extracted as 1.4 meV/V.

References and Notes

(1) Rainis, D.; Loss, D. *Phys. Rev. B* **2014**, 90(23), 235415.

(2) Kammhuber, J.; Cassidy, M. C.; Pei, F.; Nowak, M. P.; Vuik, A.; Gül, Ö.; Car, D.; Plissard, S. R.; Bakkers, E. P. a. M.; Wimmer, M.; Kouwenhoven. L. P. *Nat. Commun.* **2017**, 8(1), 478.